

钛合金表面激光熔覆原位制备 TiC/Ti₂Ni 复合涂层 微观组织及性能研究

刘亚楠¹, 谷米¹, 孙荣禄^{1,2*}, 赵宇培³, 朱玉俊^{4**}, 杨雪娇¹

¹天津工业大学机械工程学院, 天津 300387;

²天津市现代机电装备技术重点实验室, 天津 300387;

³常州大学石油化工学院江苏省绿色催化材料与技术重点实验室, 江苏 常州 213164;

⁴安徽医科大学临床医学院药学与生物工程系, 安徽 合肥 230012

摘要 为了有效改善 Ti811 合金表面硬度及耐磨性能, 利用同轴送粉法在 Ti811 表面制备了激光熔覆复合涂层。采用 X 射线衍射仪(XRD)、扫描电子显微镜(SEM)、场发射电子探针显微镜(EPMA)、维氏硬度计及摩擦磨损试验机, 系统地分析并研究了涂层的物相组成、微观组织、元素分布、显微硬度及摩擦磨损性能。结果表明: 涂层生成相主要包括 α -Ti 固溶体、陶瓷增强相 TiB₂ 和 TiC 及金属间化合物 Ti₂Ni。涂层显微硬度的提高主要归功于弥散强化及固溶强化效应, 最高可达 902 HV, 较基材显微硬度提高了 2.37 倍。涂层的磨损体积较基材下降了约 27.9%, 摩擦系数稳定在 0.38~0.42, 磨损机理主要为黏着磨损和轻微的磨粒磨损, 具有优异的耐磨性能。

关键词 激光技术; Ti811 合金; 激光熔覆; 微观组织; 显微硬度; 耐磨性能

中图分类号 TG174.44

文献标志码 A

doi: 10.3788/CJL202148.1402011

1 引言

钛合金具有比强度高、密度低及耐腐蚀性优异等特点, 在航空航天、汽车、冶金及化工等领域得到了广泛应用。然而, 低硬度和差耐磨性等缺点一直限制钛合金在耐磨工况下的使用^[1-4]。为了解决钛合金的固有缺陷, 许多表面改性技术如化学热处理(渗碳、渗氮)^[5]、离子注入^[6]、化学气相沉积和物理气相沉积^[7-8]及微弧氧化^[9]等被提出并已在提高钛合金表面性能方面取得了显著成果。随着激光技术的应用和发展, 激光表面改性技术已成为提高钛合金表面性能的研究热点, 包括脉冲激光沉积^[10]、激光冲击喷丸^[11]、激光熔化^[12]、激光合金化^[13]和激光熔覆^[14-19]。其中, 激光熔覆技术利用高能激光束辐照熔覆粉末及基材表面薄层, 二者同时熔化并在快速凝固后形成具有冶金结合强度的涂层, 该技术能够显著提高钛合金表面的硬度、耐磨性、耐腐蚀性及抗氧化性^[20-24]。

激光熔覆属于典型的非平衡凝固过程, 具有极快的加热速率和冷却速率。因此, 涂层的成型质量及力学性能受到残余热应力、高硬度陶瓷颗粒造成的低韧性和严重的裂纹敏感性等限制^[25-27]。近年来, 稀土元素的加入被证明在减小晶粒尺寸、抑制裂纹方面非常有效, 引起了研究人员的极大关注。稀土元素及其氧化物具有特殊的物理化学性质, 包括独特的电子结构、优异的化学活性和较大的离子半径, 能够影响熔池表面张力, 并在凝固过程中提供更多的形核核心来细化晶粒^[2]。Liu 等^[28]研究了 CeO₂ 含量对 Ti811 合金表面激光熔覆复合涂层组织及性能的影响, 结果表明, CeO₂ 可以细化涂层组织并有效抑制裂纹的产生, 具有弥散强化及细晶强化效应, 提高了涂层的显微硬度及耐磨性能。Feng 等^[29]研究了 LaB₆ 含量对 TC4 合金表面激光熔覆 (Ti₃Al+TiB)/Ti 基复合涂层微观结构及性能的影响, 发现纳米 La₂O₃ 对 TiB 陶瓷相具有显著的异质

收稿日期: 2020-12-10; 修回日期: 2021-01-08; 录用日期: 2021-02-07

基金项目: 国家自然科学基金(51371125)、安徽医科大学临床医学院校级科研基金(2020XJ021)

通信作者: *rlsun@tjpu.edu.cn; **675096471@qq.com

形核效应,提高了 TiB 的形核率。 La_2O_3 的加入降低了涂层残余应力,提高了显微硬度及抗氧化性能。Zhang 等^[30]研究了 Y_2O_3 含量对 TC4 合金表面激光熔覆多道涂层微观组织及性能的影响,结果表明,添加 Y_2O_3 能够细化涂层组织,当 Y_2O_3 的质量分数为 3% 时,涂层具有最佳的耐磨性能。

Ti811 合金作为民航发动机压气机叶片的重要组成部分,可在高温工作环境下长期使用,除了具有良好的焊接性能和高温性能外,还具有较高的杨氏模量、低密度和优良的振动阻尼性能^[28]。然而, Ti811 合金表面硬度低、耐磨性差等缺点限制了其广泛应用。为了提高其表面硬度和耐磨性,本文采用同轴送粉激光熔覆技术,在 Ti811 合金表面制备了激光熔覆原位自生 TiC/Ti₂Ni 复合涂层,对涂层的微观组织结构进行了表征,研究了涂层物相组成及元素分布,对涂层的显微硬度及摩擦磨损性能进行了测试,旨在为 Ti811 合金表面激光熔覆复合涂层的研究提供一定的参考。

2 试 验

2.1 试验材料

试验基材选用 Ti811 (Ti-8Al-1Mo-1V) 合金,其尺寸为 40 mm × 30 mm × 8 mm,化学成分如表 1 所示。基材表面采用喷砂方式去除污染物及氧化物,之后用无水乙醇清洗,干燥后待用。激光熔覆粉末的化学成分(质量分数)为 Ni60 (74%), TC4 (20%), NiCr-Cr₃C₂ (5%), CeO₂ (1%)。其中,高硬度的 Ni60 自熔性合金粉末的熔点较低且润湿性优良,有利于提高涂层的耐磨性能;TC4 粉末与基材具有良好的相容性;NiCr-Cr₃C₂ 主要由 (Cr, Ni) 及 Cr₃C₂ 组成, (Cr, Ni) 具有良好的耐热耐蚀性能, Cr₃C₂ 硬度高且耐磨性能优良;稀土氧化物 CeO₂ 具有抑制裂纹萌生及细化组织的作用,有利于提高涂层的硬度及耐磨性能。图 1 为粉末的扫描电子显微镜 (SEM) 形貌,可以看出,所用粉末均呈球状且球形度良好。

表 1 Ti811 基材的化学成分

Table 1 Chemical compositions of Ti811 substrate

Chemical composition	Al	Mo	V	Fe	C	N	O	Ti
Mass fraction /%	8.10	1.05	0.99	0.05	0.03	0.01	0.06	Bal.

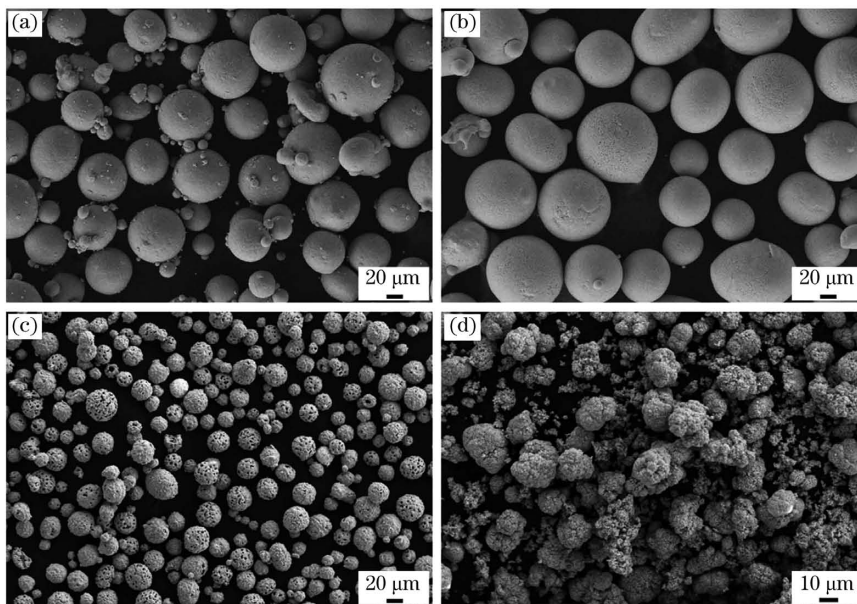


图 1 粉末形貌图。(a) TC4 粉末; (b) Ni60 粉末; (c) NiCr-Cr₃C₂ 粉末; (d) CeO₂ 粉末

Fig. 1 Morphologies of powders; (a) TC4 powder; (b) Ni60 powder; (c) NiCr-Cr₃C₂ powder; (d) CeO₂ powder

2.2 激光加工及性能测试

激光熔覆试验采用 Trulaser Cell 7040 激光加工中心,配备连续工作模式且波长为 1030 nm 的 4 kW 碟片激光器。图 2 为激光熔覆加工系统及同轴送粉法示意图,激光熔覆加工工艺参数如表 2 所

示,其中 X 代表激光头的运动方向。采用 D8 型 X 射线衍射仪 (XRD) 分析涂层物相组成,仪器采用 Cu K_α 靶材,设置加速电压为 40 kV 及电流为 150 mA,衍射速度为 10 (°)/min。利用场发射扫描电子显微镜 (FESEM) 二次电子 (SE) 模式分析涂

层的显微组织,加速电压设置为 5 kV。利用场发射电子探针显微镜(EPMA)分析涂层各元素的分布状况,加速电压为 15 kV,测试时间为 2 h。采用维氏显微硬度计测试涂层及基材的显微硬度,加载载荷为 5.0 N,加载时间为 10 s。利用 Rtec 多功能摩擦磨损试验机对基材及涂层的耐磨性能进行

了测试,摩擦副是直径为 9.5 mm 的 WC 球,试验加载载荷为 50 N,测试时间为 200 s。利用扫描电子显微镜观察并分析了基材及涂层磨损表面形貌。利用 Phase Shift MicroXAM-3D 非接触式白光干涉轮廓仪测量了基材和涂层的磨损体积及磨损轮廓。

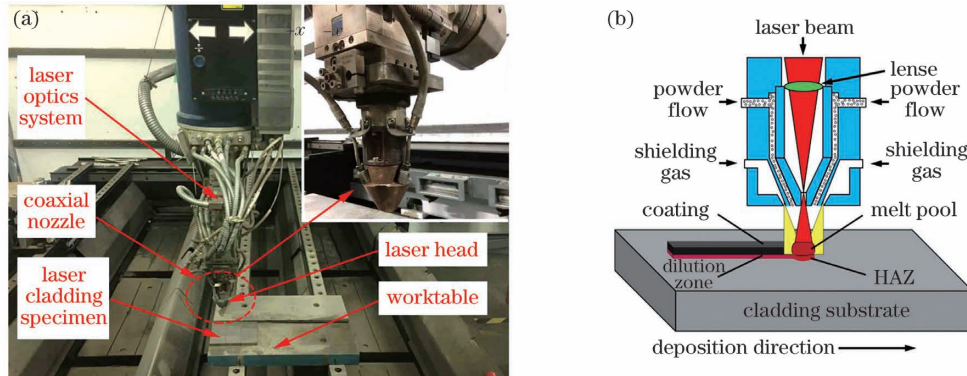


图 2 激光加工系统。(a)激光熔覆加工系统;(b)激光熔覆同轴送粉法示意图

Fig. 2 Laser processing system. (a) Laser cladding processing system; (b) schematic of synchronous powder feeding method for laser cladding

表 2 激光熔覆加工工艺参数

Table 2 Process parameters for laser cladding

Parameter	Value
Laser power /W	900
Scan speed /($\text{mm} \cdot \text{min}^{-1}$)	400
Spot diameter /mm	3.0
Overlap ratio /%	50
Powder feed rate /($\text{g} \cdot \text{min}^{-1}$)	5.0
Carrier gas flow rate (He) /($\text{L} \cdot \text{min}^{-1}$)	7.0
Shielding gas flow rate (Ar) /($\text{L} \cdot \text{min}^{-1}$)	11.0
Working distance /mm	16.0

3 结果及分析

3.1 物相分析

图 3 为试验所用熔覆粉末的 XRD 图谱分析结果。由图 3(a)~(d)可知,Ni60 自熔性合金粉末主要由 γ -Ni、 Ni_3B 、CrB、 Cr_2B 和 Cr_{23}C_6 等金属间化合物组成,TC4 粉末主要由 α -Ti 和 β -Ti 组成,NiCr-Cr₃C₂ 粉末主要由 (Cr, Ni) 和 Cr₃C₂ 组成,CeO₂ 粉末中未检测到其他杂质。XRD 检测结果显示,激光熔覆粉末未检测到杂质及其他氧化物,表明所用粉末均具有较高纯度。

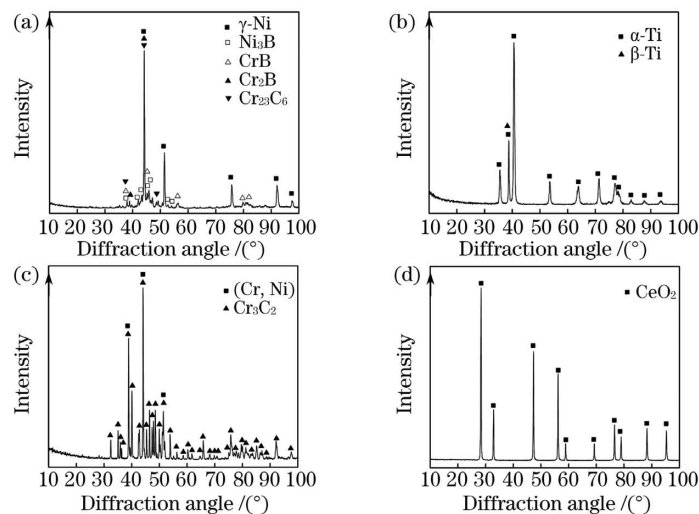
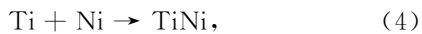
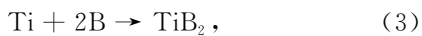


图 3 粉末 XRD 分析结果。(a)Ni60 粉末;(b)TC4 粉末;(c)NiCr-Cr₃C₂ 粉末;(d)CeO₂ 粉末

Fig. 3 XRD analysis results of powders; (a) Ni60 powder; (b) TC4 powder; (c) NiCr-Cr₃C₂ powder; (d) CeO₂ powder

在激光熔覆过程中, Ti811 合金表面与熔覆粉末在能量激光束辐照作用下迅速熔化形成熔池, 并伴随复杂的物理化学反应。在激光连续扫描作用下, 熔池在快速凝固过程中形成多种物相, 涂层的 XRD 衍射分析结果如图 4(a) 所示, 可以看出, 涂层生成相主要由 α -Ti、TiC、TiB₂ 和 Ti₂Ni 组成。此外, 检测到较弱的 CeO₂ 衍射峰, 表面涂层中存在少量的 CeO₂。基于 XRD 标定结果及体系的元素组成, 熔池内可能发生的反应为



根据热力学数据^[31], 确定了各个反应的吉布斯自由能 (ΔG) 与温度 (T) 之间的函数关系, 如图 4(b) 所示。由计算结果可知, (1)~(6) 式的 ΔG

均为负值, 表明所有反应均可自发形成。

在涂层生成物相中, TiB₂ 和 TiC 具有较高的熔点 (3250 °C 和 3067 °C) 和较低的 ΔG 。因此, TiB₂ 和 TiC 会优先从熔池中析出。与 TiB 相比, TiB₂ 具有更低的 ΔG , 熔池内会优先生成 TiB₂, 结合图 4(a) 可知, 熔池内并没有发生 (2) 式所示的反应。根据 Ti-Ni 二元相图^[32], 当温度降至 1310 °C 左右时将析出 TiNi。当温度进一步降低到 984 °C 时, TiNi 和 Ti 将通过包晶反应生成 Ti₂Ni。由图 4(b) 计算结果可知, TiNi₃ 的 ΔG 小于 Ti₂Ni 和 TiNi, 然而研究表明, Ti₂Ni 具有 Ti-Ni 体系中最稳定的晶体结构^[33]。根据图 4(a) 中的标定结果可知, 涂层最终形成了 Ti₂Ni 相, 而非其他 Ti-Ni 系金属间化合物。最终, β -Ti 转变为 α -Ti 发生在 882 °C 左右。综上可知, 涂层内最终存在的增强相为 TiB₂、TiC、Ti₂Ni 及 α -Ti, 且三者的析出顺序为 TiB₂ → TiC → Ti₂Ni → α -Ti, 分析过程如图 4(c) 所示。

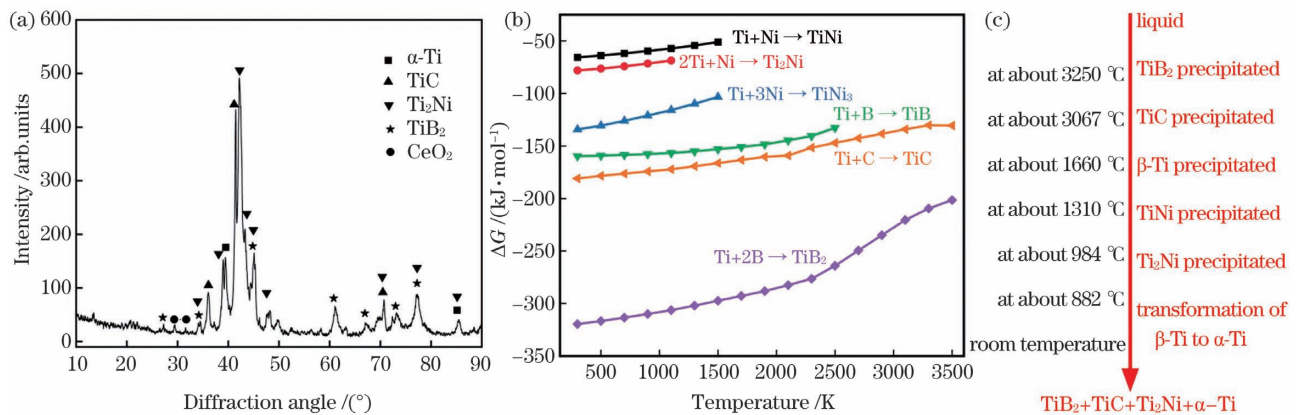


图 4 涂层物相及反应分析。(a) 涂层的 XRD 图谱; (b) 不同反应的 ΔG 随 T 的变化曲线; (c) 物相反应析出顺序示意图

Fig. 4 Phase and reaction analysis of coating. (a) XRD image of coating; (b) ΔG versus T for different reactions;

(c) schematic of phase precipitation sequence

3.2 微观组织和能谱分析

图 5(a)、(b) 为涂层横截面 SEM 形貌, 可以发现, 涂层分为三个区域: 熔覆区 (CZ)、结合区 (BZ) 及热影响区 (HAZ)。由图 5(b) 可以看出, 在涂层和基材 Ti811 之间形成了一条结合线 (bonding line), 表明涂层与基材结合良好。此外, 在涂层附近的热影响区观察到了针状马氏体, 这是由于激光熔覆极快的冷却速度超过了基材临界冷却速度。图 5(c)、(d) 显示了复合涂层的微观结构。由图 5 可知, 涂层主要由花瓣状相、条状相、棒状相及基底相组成。

图 6 为涂层物相的能谱分析 (EDS) 结果。由分析结果可知, 花瓣状相主要由 Ti 和 C 元素组成, 且其原子数分数比约为 1 : 1。结合 XRD 标定结果可知, 花瓣状相被确定为增强相 TiC。在条状相中, Ti 与 Ni 的原子数分数比为 1 : 2, 条状相为金属间化合物 Ti₂Ni。棒状相的能谱分析结果表明, 其主要含有 Ti 和 B 元素, 且两者的原子数分数比约为 1 : 2, 棒状相为增强相 TiB₂。基底相主要由 Ti、Ni、Cr 及 Al 等元素组成, 其中 Ti 元素的质量分数超过 80%, 基底相为 α -Ti 固溶体。

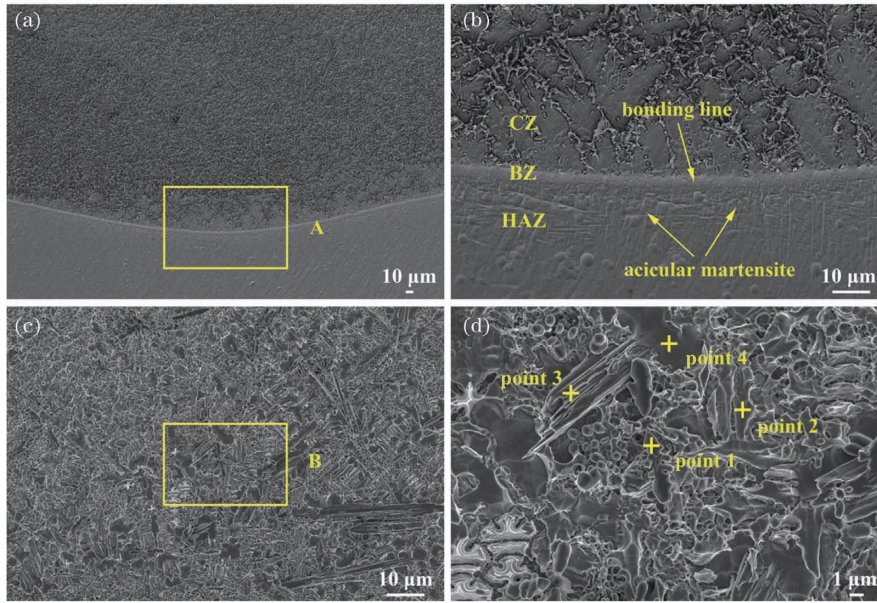


图 5 涂层形貌及微观组织图。(a)涂层结合区形貌；(b)图 5(a)中 A 区域的放大图；(c)涂层的微观组织；(d)图 5(c)中 B 区域的放大图

Fig. 5 Morphologies and microstructures of coating. (a) Morphology of coating bonding zone; (b) enlarged view of area A in Fig.5(a); (c) microstructure of coating; (d) enlarged view of area B in Fig.5(c)

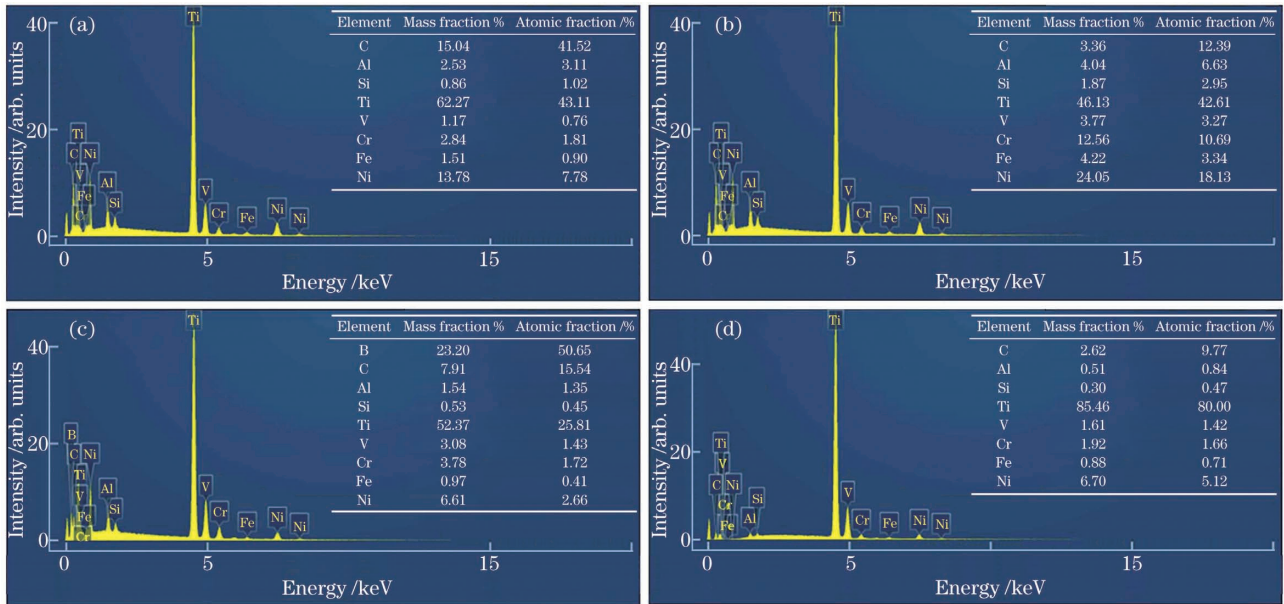


图 6 涂层物相的 EDS 结果。(a) TiC; (b) Ti₂Ni; (c) TiB₂; (d) α-Ti

Fig. 6 EDS results of coating phases. (a) TiC; (b) Ti₂Ni; (c) TiB₂; (d) α-Ti

3.3 电子探针分析

为了明确涂层中各元素的分布状况,对涂层进行了面扫描,EPMA 检测结果如图 7 所示。由图 7 可知,涂层生成相的主要特征分别为花瓣状、棒状和条状相,与 SEM 观察结果一致。根据检测结果可知,花瓣状相富含 Ti 和 C,棒状相主要成分为 Ti 和 B 元素,带状相主要含有 Ti 和 Ni 元素,固

溶体相富含 Ti 元素并伴有 Ni、Cr 及 Al 等元素。结合图 4(a)及图 6,可以确定涂层生成相为花瓣状 TiC、棒状 TiB₂、条状 Ti₂Ni 及固溶体 α-Ti。此外,发现白色纳米颗粒弥散分散于涂层中,根据 Ce 和 O 元素的元素分布图及 XRD 标定分析结果,可以确定其为纳米 CeO₂ 颗粒,在涂层中具有弥散强化效应^[2]。

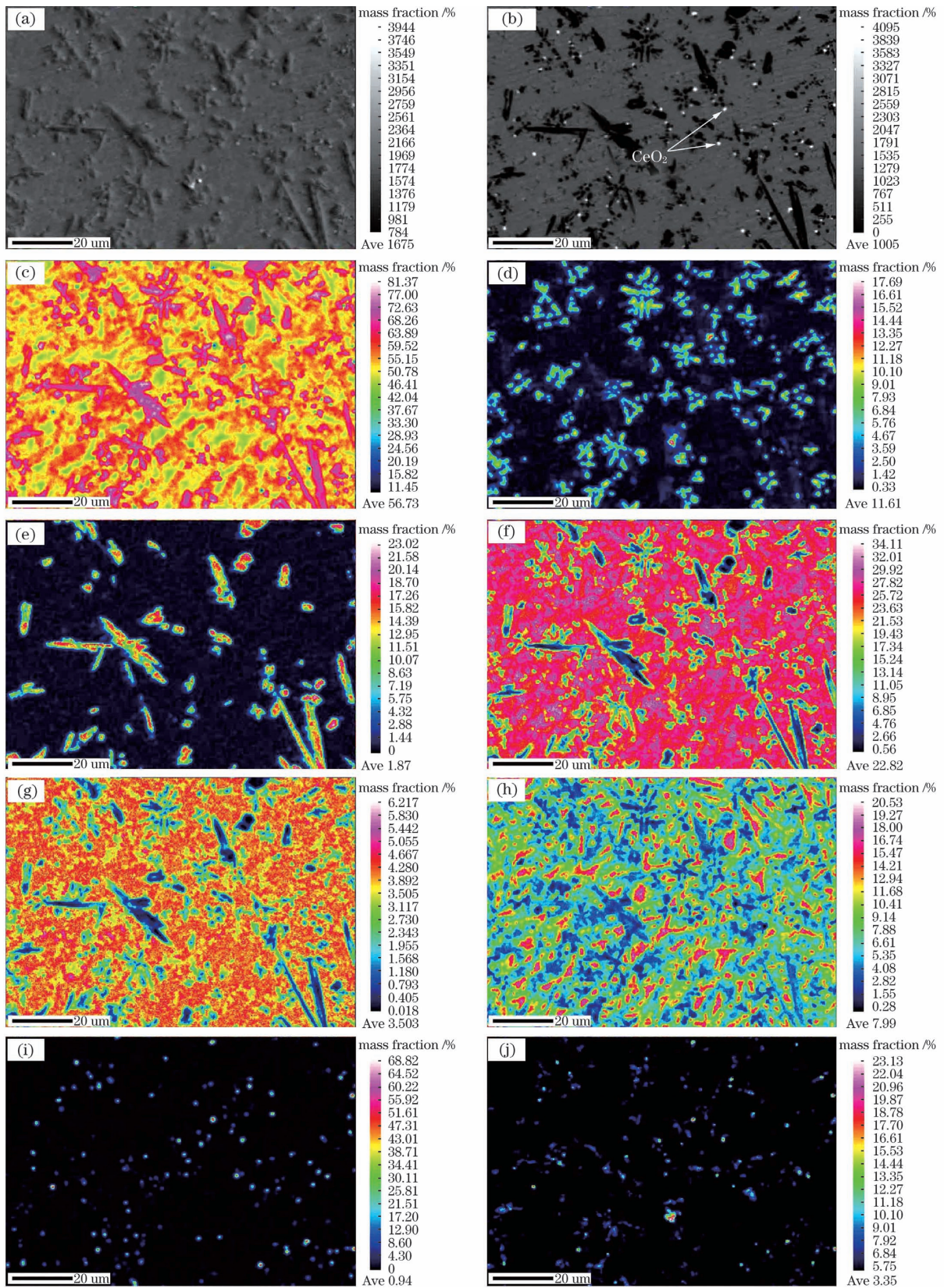


图 7 涂层的微观组织及元素分布图。(a)SE 图像;(b)背散射电子图像;(c)Ti 分布;(d)C 分布;(e)B 分布;(f)Ni 分布;
(g)Al 分布;(h)Cr 分布;(i)Ce 分布;(j)O 分布

Fig. 7 Microstructures of coating and elemental distribution map. (a) SE image; (b) backscattered electron image; (c) distribution of Ti; (d) distribution of C; (e) distribution of B; (f) distribution of Ni; (g) distribution of Al; (h) distribution of Cr; (i) distribution of Ce; (j) distribution of O

4 显微硬度

图 8 为沿涂层横截面深度方向的显微硬度分布曲线,显微硬度整体呈逐渐下降趋势,以硬度值分布状况为依据把熔覆层划分为涂层(Coating)、热影响区和基体(Substrate)三部分。由图 8 可知,涂层的显微硬度(837~902 HV)高于基材 Ti811 的显微硬度(380 HV 左右),提升了 2.37 倍。涂层显微硬度提高的原因主要为:熔池凝固过程中形成了大量高硬度的陶瓷增强相 TiC、TiB₂ 及金属间化合物 Ti₂Ni,它们具有弥散强化作用;涂层中纳米 CeO₂ 具有弥散强

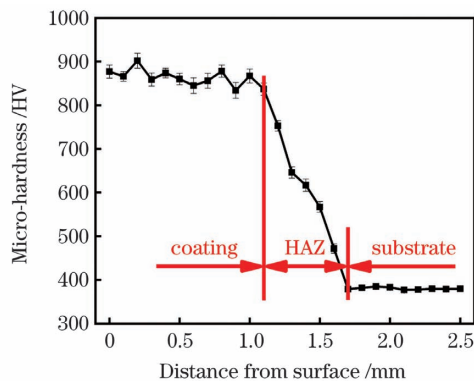


图 8 涂层显微硬度分布图

Fig. 8 Micro-hardness distribution of coating

化作用;Ni、Al、Cr 及 Ti 等元素固溶于 α -Ti 中,具有固溶强化作用。因此,涂层显微硬度的提高归功于弥散强化及固溶强化效应的共同作用。

5 摩擦磨损性能

图 9(a)、(c)为 Ti811 合金的白光干涉三维形貌图及摩擦磨损 SEM 形貌图。可以看出,Ti811 合金磨损表面粗糙,平整度较差,存在深且宽的沟槽、碎屑及脱层现象,表明基材经历了较为严重的磨损。在摩擦磨损试验过程中,摩擦副 WC 球表面凸起的微硬质很容易渗入进硬度相对较软的基材表面,导致变形和微切削。因此,基材磨损表面出现较为严重的磨粒和黏着磨损特征。图 9(b)、(d)为涂层的白光干涉三维形貌图及摩擦磨损 SEM 形貌图,与基材相比,其磨损表面较为平坦并伴随浅且窄的沟槽,磨粒尺寸及数量显著减小,碎屑和脱层现象得到了显著改善。这是由于涂层显微硬度的较高能够有效提高涂层的抗变形能力。此外,涂层中原位生成的大量增强相,如 TiC、TiB₂ 及 Ti₂Ni,在摩擦磨损过程中承担了主要载荷,有效阻止了磨损和变形。基于以上分析,涂层主要的磨损机制为黏着磨损和轻微的磨粒磨损。

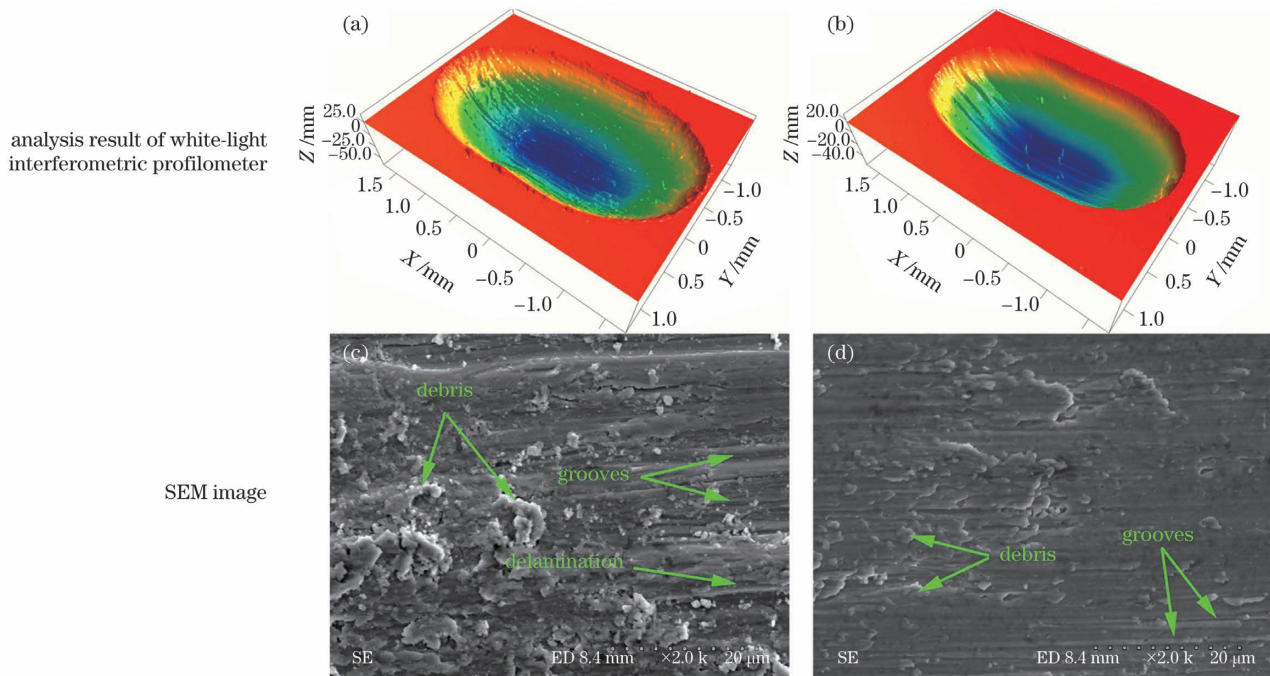


图 9 白光干涉轮廓仪分析结果及磨损表面 SEM 图。(a)(c)基材 Ti811; (b)(d)涂层

Fig. 9 Analysis results by white-light interferometric profilometer and SEM images of wear surfaces. (a)(c) Ti811 substrate; (b)(d) coating

图 10(a)、(b)分别为基材 Ti811 和涂层的磨损体积曲线图。可以看出,涂层的磨损体积为

0.1718 mm³,较基材的磨损体积(0.2383 mm³)下降了约 27.9%。表明在相同的摩擦磨损试验条件

下,涂层具有更好的耐磨性能。图 10(c)为基材 Ti811 和涂层的摩擦系数对比曲线,可见基材 Ti811 的摩擦系数较高,波动范围为 0.56~0.75,波动范围较大。相比之下,涂层的摩擦系数较低且相对稳定,波动范围为 0.38~0.42。图 10(d)为基材 Ti811 和涂层的磨损轮廓对比曲线,可见

涂层的横截面磨损深度及磨损面积均小于基材 Ti811,在与摩擦副相互作用过程中,涂层原位生成的增强相可以有效抵抗 WC 球的不断挤压,具有“骨架”作用。对比基材 Ti811 与涂层的显微硬度分析及摩擦磨损试验分析可以得出,涂层具有优异的耐磨性能。

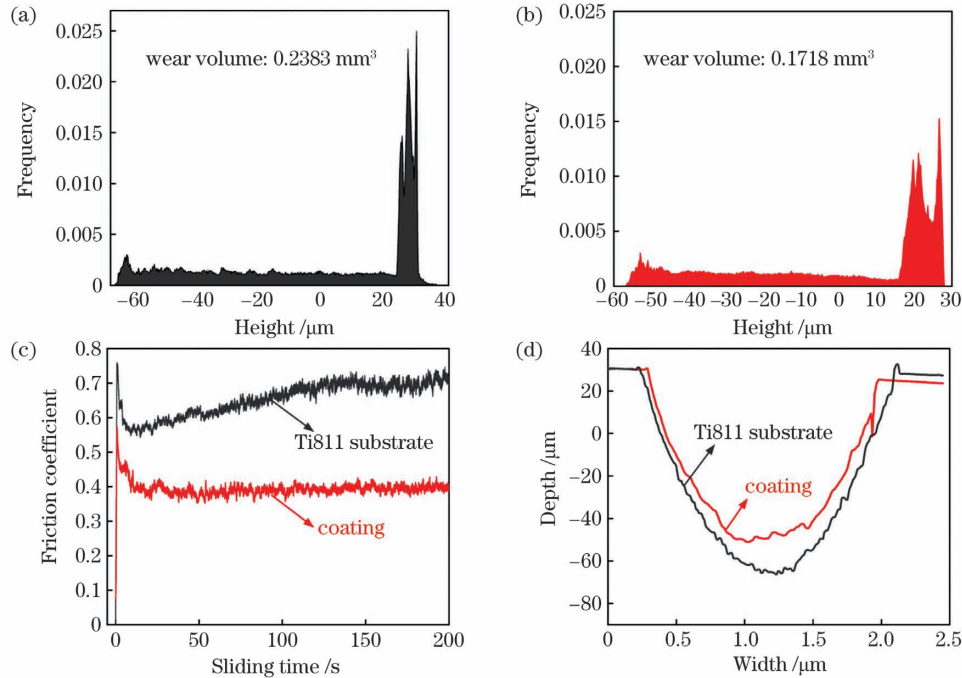


图 10 涂层的摩擦磨损性能。(a)基材 Ti811 磨损体积;(b)涂层磨损体积;(c)基材 Ti811 与涂层的摩擦系数对比;
(d)基材 Ti811 与涂层的磨损轨迹截面轮廓对比

Fig. 10 Friction and wear properties of coating. (a) Wear volume of Ti811 substrate; (b) wear volume of coating;
(c) friction coefficient comparison of Ti811 substrate and coating; (d) wear track profile comparison of Ti811 substrate and coating

6 结 论

利用同轴送粉激光熔覆技术,在 Ti811 合金表面制备了激光熔覆原位自生 TiC/Ti₂Ni 复合涂层,涂层最终生成相主要包含陶瓷增强相 TiC 和 TiB₂、金属间化合物 Ti₂Ni 及 α-Ti 固溶体,增强相的析出顺序为 TiB₂→TiC→Ti₂Ni→α-Ti。涂层显微硬度的提高主要归功于增强相 TiC、TiB₂、Ti₂Ni 和纳米 CeO₂ 的弥散强化效应及 α-Ti 的固溶强化效应。涂层显微硬度最高为 902 HV,约为 Ti811 合金硬度的 2.37 倍。涂层的磨损体积较基材 Ti811 减少了约 27.9%,涂层的摩擦系数稳定在 0.38~0.42 区间,其磨损机制主要为黏着磨损和轻微的磨粒磨损,涂层具有优良的耐磨性能。

参 考 文 献

[1] Ping X L, Fu H G, Sun S T, et al. Progress in

preparation of hard phase reinforced Ni-based alloy composite coating by laser cladding [J]. Materials Reports, 2019, 33(9): 1535-1540.

平学龙,符寒光,孙淑婷,等.激光熔覆制备硬质颗粒增强镍基合金复合涂层的研究进展[J].材料导报,2019,33(9):1535-1540.

[2] Hao F, Xin S W, Mao Y C, et al. Review on application of titanium alloy in armor [J]. Materials Reports, 2020, 34(S1): 293-296,327.

郝芳,辛社伟,毛友川,等.钛合金在装甲领域的应用综述[J].材料导报,2020,34(S1):293-296,327.

[3] Zhang J H, Li X X, Xu D S, et al. Recent progress in the simulation of microstructure evolution in titanium alloys [J]. Progress in Natural Science: Materials International, 2019, 29(3): 295-304.

[4] Gangwar K, Ramulu M. Friction stir welding of titanium alloys: a review [J]. Materials & Design, 2018, 141: 230-255.

[5] Sarma J, Kumar R, Sahoo A K, et al. Enhancement

- of material properties of titanium alloys through heat treatment process: a brief review [J]. *Materials Today: Proceedings*, 2020, 23(Part 3): 561-564.
- [6] Vlcek P, Fojt J, Weiss Z, et al. The effect of nitrogen saturation on the corrosion behaviour of Ti-35Nb-7Zr-5Ta beta titanium alloy nitrided by ion implantation[J]. *Surface and Coatings Technology*, 2019, 358: 144-152.
- [7] An Q L, Chen J, Tao Z R, et al. Experimental investigation on tool wear characteristics of PVD and CVD coatings during face milling of Ti-6242S and Ti-555 titanium alloys [J]. *International Journal of Refractory Metals and Hard Materials*, 2020, 86: 105091.
- [8] Haron C H C, Ginting A, Arshad H, et al. Performance of alloyed uncoated and CVD-coated carbide tools in dry milling of titanium alloy Ti-6242S [J]. *Journal of Materials Processing Technology*, 2007, 185(1/2/3): 77-82.
- [9] Wang Y, Yu H J, Chen C Z, et al. Review of the biocompatibility of micro-arc oxidation coated titanium alloys [J]. *Materials & Design*, 2015, 85: 640-652.
- [10] Wang D G, Chen C Z, Jin Q P, et al. HA/Bioglass composite films deposited by pulsed laser with different substrate temperature [J]. *Applied Physics A*, 2014, 114(3): 897-902.
- [11] Ganesh P, Sundar R, Kumar H, et al. Studies on fatigue life enhancement of pre-fatigued spring steel specimens using laser shock peening [J]. *Materials & Design*, 2014, 54: 734-741.
- [12] Balla V K, Soderlind J, Bose S, et al. Microstructure, mechanical and wear properties of laser surface melted Ti6Al4V alloy [J]. *Journal of the Mechanical Behavior of Biomedical Materials*, 2014, 32: 335-344.
- [13] Guo C, Zhou J S, Zhao J R, et al. Microstructure and friction and wear behavior of laser boronizing composite coatings on titanium substrate [J]. *Applied Surface Science*, 2011, 257(9): 4398-4405.
- [14] Kooi B J, Pei Y T, de Hosson J T M, et al. The evolution of microstructure in a laser clad TiB-Ti composite coating [J]. *Acta Materialia*, 2003, 51(3): 831-845.
- [15] Liu Y N, Sun R L, Zhang T G, et al. Microstructures and properties of laser cladding coating on Ti811 alloy surface [J]. *Surface Technology*, 2019, 48(2): 123-132.
刘亚楠, 孙荣禄, 张天刚, 等. Ti811 合金表面激光熔覆涂层微观组织及性能研究 [J]. *表面技术*, 2019, 48(2): 123-132.
- [16] Qiu Y, Zhang F Y, Hu T T, et al. Effect of laser power on microstructure and hardness of Ti40 flame-retardant titanium alloy deposited by laser cladding on TC4 surface [J]. *Chinese Journal of Lasers*, 2019, 46(11): 1102011.
邱莹, 张凤英, 胡腾腾, 等. 激光功率对 TC4 表面熔覆 Ti40 阻燃钛合金组织及硬度的影响 [J]. *中国激光*, 2019, 46(11): 1102011.
- [17] Zhang T G, Zhuang H F, Xiao H Q, et al. Effect of rare earth on microstructure and friction and wear properties of Ti-based laser cladding layer [J]. *Chinese Journal of Lasers*, 2019, 46(9): 0903001.
张天刚, 庄怀风, 肖海强, 等. 稀土对 Ti 基激光熔覆层组织与摩擦磨损性能的影响 [J]. *中国激光*, 2019, 46(9): 0903001.
- [18] Lü Y H, Li J, Tao Y F, et al. Oxidation behaviors of the TiNi/Ti₂Ni matrix composite coatings with different contents of TaC addition fabricated on Ti₆Al₄V by laser cladding [J]. *Journal of Alloys and Compounds*, 2016, 679: 202-212.
- [19] Liu Y N, Sun R L, Niu W, et al. Microstructure and friction and wear resistance of laser cladding composite coating on Ti811 surface [J]. *Chinese Journal of Lasers*, 2019, 46(1): 0102010.
刘亚楠, 孙荣禄, 牛伟, 等. Ti811 表面激光熔覆复合涂层的微观组织及摩擦磨损性能 [J]. *中国激光*, 2019, 46(1): 0102010.
- [20] Sun R L, Lei Y W. Microstructure and hardness of laser clad SiC_p-Al composite coatings on Al alloys [J]. *Materials Letters*, 2008, 62(17/18): 3272-3275.
- [21] Lei Y W, Sun R L, Tang Y, et al. Numerical simulation of temperature distribution and TiC growth kinetics for high power laser clad TiC/NiCrBSiC composite coatings [J]. *Optics & Laser Technology*, 2012, 44(4): 1141-1147.
- [22] Lei Y W, Sun R L, Tang Y, et al. Microstructure and phase transformations in laser clad Cr_xS_y/Ni coating on H13 steel [J]. *Optics and Lasers in Engineering*, 2015, 66: 181-186.
- [23] Gao Y L, Wang C S, Yao M, et al. The resistance to wear and corrosion of laser-cladding Al₂O₃ ceramic coating on Mg alloy [J]. *Applied Surface Science*, 2007, 253(12): 5306-5311.
- [24] Xu B S, Fang J X, Dong S Y, et al. Heat-affected zone microstructure evolution and its effects on mechanical properties for laser cladding FV520B stainless steel [J]. *Acta Metallurgica Sinica*, 2016, 52(1): 1-9.
徐滨士, 方金祥, 董世运, 等. FV520B 不锈钢激光熔覆热影响区组织演变及其对力学性能的影响 [J].

- 金属学报, 2016, 52(1): 1-9.
- [25] Farahmand P, Liu S, Zhang Z, et al. Laser cladding assisted by induction heating of Ni-WC composite enhanced by nano-WC and La_2O_3 [J]. *Ceramics International*, 2014, 40(10): 15421-15438.
- [26] Dong S Y, Yan X L, Xu B S, et al. Influence of microstructure and residual stress on surface stress measurement of laser cladding layer by Rayleigh wave [J]. *Journal of Mechanical Engineering*, 2015, 51(24): 50-56.
- 董世运, 闫晓玲, 徐滨士, 等. 微观组织及残余应力对瑞利波评价激光熔覆层应力的影响[J]. *机械工程学报*, 2015, 51(24): 50-56.
- [27] Liu Y N, Yang L J, Yang X J, et al. Optimization of microstructure and properties of composite coatings by laser cladding on titanium alloy [J]. *Ceramics International*, 2021, 47(2): 2230-2243.
- [28] Liu Y N, Sun R L, Niu W, et al. Effects of CeO_2 on microstructure and properties of TiC/Ti₂Ni reinforced Ti-based laser cladding composite coatings [J]. *Optics and Lasers in Engineering*, 2019, 120: 84-94.
- [29] Feng Y Q, Feng K, Yao C W, et al. Effect of LaB_6 addition on the microstructure and properties of (Ti₃Al + TiB)/Ti composites by laser cladding [J]. *Materials & Design*, 2019, 181: 107959.
- [30] Zhang T G, Zhuang H F, Zhang Q, et al. Influence of Y_2O_3 on the microstructure and tribological properties of Ti-based wear-resistant laser-clad layers on TC4 alloy [J]. *Ceramics International*, 2020, 46(9): 13711-13723.
- [31] Barin I, Sauert F, Rhonhof S E, et al. *Thermochemical data of pure substances* [M]. 3rd ed. Hoboken: John Wiley & Sons, 1995.
- [32] Massalski T B, Okamoto H, Subramanian P R, et al. *Binary alloy phase diagrams* [M]. 2nd ed. Geauga: American Society for Metals, 1986.
- [33] Wang P, Li J, Lin C Z, et al. First-principles calculations of electronic structure and mechanical properties of Ti-Ni intermetallic compounds [J]. *The Chinese Journal of Nonferrous Metals*, 2016, 26(12): 2546-2554.
- 王鹏, 李军, 林崇智, 等. Ti-Ni 金属间化合物电子结构与力学性质的第一性原理计算 [J]. *中国有色金属学报*, 2016, 26(12): 2546-2554.

Microstructure and Properties of *In-situ* TiC/Ti₂Ni Composite Coating Prepared via Laser Cladding on Titanium Alloy

Liu Yanan¹, Gu Mi¹, Sun Ronglu^{1,2*}, Zhao Yupei³, Zhu Yujun^{4**}, Yang Xuejiao¹

¹*School of Mechanical Engineering, Tiangong University, Tianjin 300387, China;*

²*Tianjin Area Major Laboratory of Advanced Mechatronics Equipment Technology, Tianjin 300387, China;*

³*Jiangsu Key Laboratory of Green Catalytic Materials and Technology, School of Petrochemical Engineering, Changzhou University, Changzhou, Jiangsu 213164, China;*

⁴*Department of Pharmacy and Biomedical Engineering, Clinic College, Anhui Medical University, Hefei, Anhui 230012, China*

Abstract

Objective Titanium alloys have low density, high specific strength, and excellent corrosion resistance, thus they are commonly used in the engineering field to improve the mechanical properties of structural parts. However, their usage for various industrial applications is severely constrained owing to low hardness and poor wear properties. Several critical studies have been conducted regarding the surface modification of titanium alloys to solve their defects, including thermal spray, ion implantation, vapor deposition, and laser cladding, which have effectively improved their mechanical properties. In this work, a laser cladding composite coating was prepared on the Ti811 surface using the coaxial powder feeding method to improve the micro-hardness and wear resistance of the Ti811 alloy. The coating microstructure was characterized to study its phase compositions and elemental distribution. Moreover, the micro-hardness, friction, and wear properties of the coating were tested, and the CeO_2 dispersive strengthening mechanism in the coating was revealed. The research results here can provide a valuable experimental and analysis basis for studying the laser cladding of composite coatings on Ti811 alloys.

Methods The TruLaser Cell 7040 laser-processing center with a 4 kW laser at a 1030 nm wavelength was used for the laser cladding process. The coaxial powder feeding laser cladding technology was developed to synthesize the

TiC/Ti₂Ni composite coating. The laser process parameters are as follows: laser power of 900 W, scanning speed of 400 mm/min, powder feeding speed of 5.0 g/min, protective gas flow of 11 L/min, powder feeding gas flow of 7 L/min, spot diameter of 3 mm, and working distance of 16 mm. The chemical compositions (mass fractions) of the materials used for laser cladding are Ni60 (74%), TC4 (20%), NiCr-Cr₃C₂ (5%), and CeO₂ (1%). A Ti811 (Ti-8Al-1Mo-1V) cuboid specimen of 40 mm × 30 mm × 8 mm was used as the substrate material. The chemical compositions (mass fractions) of the substrate are Al (8.1%), Mo (1.05%), V (0.99%), Fe (0.05%), C (0.03%), N (0.01%), O (0.06%), and Ti (Bal.). Before laser cladding, the working surfaces of the specimens were sandblasted to remove the oxide skin and cleaned in absolute ethanol using an ultrasonic cleaner for 20 min. The specimens were then cut off along the section of the coating via wire cut electrical discharge machining into a size of 15 mm × 7 mm × 8 mm as the metallographic samples. A mixture of HF, HNO₃, and H₂O was used as the etchant. The etching time was 10–25 s. The precipitation order of the phases was predicted using thermodynamic calculation. X-ray diffraction, scanning electron microscope (SEM), field emission electron probe (EPMA), Vickers hardness, friction, and wear testers were used to analyze and study the phase compositions, microstructures, elemental distributions, micro-hardness, and wear resistance of the coating.

Results and Discussions The composition analysis showed that the final phase mainly consisted of ceramic-reinforced phase TiC and TiB₂, intermetallic compound Ti₂Ni, and α-Ti solid solution. The thermodynamic calculation revealed a precipitation order of TiB₂ → TiC → Ti₂Ni → α-Ti (Fig. 4). The SEM analysis and the EPMA results showed that TiC had a petal shape, TiB₂ had a long rod shape, Ti₂Ni had a strip shape, and nano-CeO₂ was dispersed in the coating (Figs. 5 and 7). The micro-hardness improvement was mainly attributed to the effect of fine grain strengthening, dispersion strengthening, and solution strengthening. The highest micro-hardness of the coating was 902 HV, 2.37 times that of the Ti811 substrate (Fig. 8). The wear volume of the coating was reduced by 27.9% compared with that of the substrate. The friction coefficient was stable between 0.38 and 0.42. The wear mechanism was mainly adhesive and slight abrasive wear with an excellent wear resistance (Figs. 9 and 10).

Conclusions In this study, an *in-situ* TiC/Ti₂Ni composite coating was prepared on Ti811 alloy using the coaxial powder feeding laser cladding technology. The final phase of the coating mainly consists of ceramic-reinforced TiC and TiB₂, intermetallic compound Ti₂Ni, and α-Ti solid solution. The precipitation order of this phase was TiB₂ → TiC → Ti₂Ni → α-Ti. The improvement in the coating micro-hardness was mainly attributed to the dispersion strengthening effects of TiC, TiB₂, Ti₂Ni, and nano-CeO₂, and the solid solution strengthening effect of α-Ti. The highest coating micro-hardness was 902 HV, which is approximately 2.37 times that of the Ti811 alloy. The wear volume of the coating was approximately 27.9% less than that of the substrate. The friction coefficient of the coating was stable between 0.38 and 0.42. The wear mechanism of the coating was dominated by adhesive wear and slight abrasive wear with excellent wear resistance.

Key words laser technique; Ti811 alloy; laser cladding; microstructure; micro-hardness; wear resistance

OCIS codes 140.3390; 140.3510; 140.3590